nature communications

Article | Article in Press

https://doi.org/10.1038/s41467-026-79076-6

Deep strong light-matter coupling in 3D Kane fermions without Dicke criticality

Received: 17 May 2026

Accepted: 8 October 2026

Published online: 17 November 2026

Check for updates

Dmitriy Yavorskiy[1,2] ✉, David Hagenmüller[3], Noureddine Charrouj[1], Yurii Ivonyak[1,2], Alexander Kazakov[4], Yanko Todorov[5], Wojciech Knap[1,2] & Marcin Białek[1] ✉

Deep-strong light-matter coupling is a non-perturbative regime of quantum electrodynamics in which the interaction strength exceeds the frequencies of uncoupled light and matter excitations. Whether a Dicke superradiant phase transition can occur in electronic systems with linear energy-momentum dispersion remains controversial because of the apparent absence of a diamagnetic $\mathbf{A}^2$ term in their low-energy Hamiltonian. Here, we investigate Landau polaritons in a bulk mercury cadmium telluride film hosting Kane fermions coupled to a Fabry-Perot resonator. The ultralow cyclotron mass of Kane fermions and a thermally tunable carrier density enable tuning from weak to deep-strong coupling, reaching the single-mode coupling strength of 1.6 above room temperature. Near the Dirac point (100 K), deep-strong coupling coexists with linear low-energy dispersion. Our microscopic quantum theory and classical electromagnetic simulations are in agreement with measured spectra. We conclude that a diamagnetic $\mathbf{A}^2$ term emerges despite the linear dispersion, preventing a Dicke superradiant phase transition.

Strong light-matter coupling in cavity quantum electrodynamics (QED) arises when coherent energy exchange between matter and photonic modes exceeds dissipation rates, leading to hybrid light–matter excitations known as polaritons[1,2]. In the ultrastrong coupling regime, where the vacuum Rabi frequency Ω becomes a significant fraction of the bare transition frequency ω, the rotating-wave approximation breaks down, and the ground state acquires a squeezed-vacuum character[3–5]. In the deep-strong-coupling regime ($\Omega/\omega > 1$), light–matter interactions become fully non-perturbative and generate large ground-state photon populations[3–5]. These regimes lie at the heart of polaritonics, a rapidly growing field exploring how cavity QED can reshape material properties[6–8], including phase transitions[9–11], chemical reactivity[6,12,13], as well as charge[14,15] and energy transport[16,17].

The superradiant quantum phase transition is a paradigmatic illustration of how polaritonics could push the frontier in quantum materials research. Originally predicted within the Dicke model, describing a collection of two-level systems coupled to an electromagnetic cavity mode[18], it arises when the light-matter coupling strength exceeds a critical threshold[19]. In the superradiant phase, which should appear in the deep-strong-coupling regime, the ground state exhibits both photon condensation and macroscopic matter polarisation[20]. In realistic systems, however, the diamagnetic $\mathbf{A}^2$ term imposes stringent constraints on such a phase transition[21,22], which translates into no-go theorems[23–25]. About a decade ago, it was theoretically proposed that the minimally coupled low-energy Dirac model of graphene could evade the no-go theorems and support a superradiant phase transition, because the linear momentum dependence of the Dirac Hamiltonian eliminates the conventional $\mathbf{A}^2$ term[26]. This prediction was later questioned on the grounds that gauge invariance requires the dynamical generation of an effective $\mathbf{A}^2$ term[25,27]. As a generalisation of Dirac fermions, Kane fermions offer an ideal platform for examining this issue.

[1]CENTERA Labs, Institute of High Pressure Physics, Polish Academy of Sciences, Warsaw, Poland. [2]CENTERA, CEZAMAT, Warsaw University of Technology, Warsaw, Poland. [3]Institut de Physique et Chimie des Matériaux de Strasbourg, UMR 7504, Université de Strasbourg and CNRS, Strasbourg, France. [4]International Research Centre MagTop, Institute of Physics, Polish Academy of Sciences, Warsaw, Poland. [5]Laboratoire de Physique et d'Étude des Matériaux, LPEM, UMR 8213, ESPCI Paris, Université PSL, Paris, France. ✉e-mail: dmitriy.yavorskiy@unipress.waw.pl; marcin.bialek@unipress.waw.pl

Here, we report the experimental realisation of the deep-strong-coupling regime between the photonic modes of a Fabry-Perot resonator and the cyclotron-resonance (CR) transitions between Landau levels (LLs) of 3D Kane fermions. Previous experimental realisations, such as Landau[28] or magnetoplasmon[29–31] polaritons, were reported mainly with 2D electron gas from gallium arsenide (GaAs) quantum wells with parabolic band dispersion, where the effect of the $\mathbf{A}^2$ terms is well-known[32]. More recently, Dirac-Landau polaritons with a normalised coupling strength of approximately $\Omega/\omega \approx 0.22$ were demonstrated in HgTe quantum wells[33]. This platform has enabled engineering of polaritonic nonlinearities[34], modifications of magnetotransport[35,36], quantum Hall response[37,38], and excitation spectra of quantum materials[39,40]. Deeply subwavelength metasurface resonators have enabled coupling ratios up to $\Omega/\omega = 1.4$ [41,42], whereas Fabry-Perot[43] and photonic crystal cavities[44,45] offer weaker confinement but substantially higher quality factors, opening regimes where high cooperativity coexists with ultrastrong coupling[44–46].

Experimental realisations of extreme coupling regimes in bulk 3D electronic systems remain scarce, whereas narrow-gap semiconductors with relativistic-like dispersion[47] offer a promising route. Mercury cadmium telluride ($Hg_{1-x}Cd_xTe$, MCT) is a paradigmatic example, whose band structure can be tuned by composition, temperature, or pressure through a topological phase transition via a gapless critical point[48,49]. Near this point, the conical dispersion at the Γ point intersects a nearly flat heavy-hole band, yielding a bulk analogue of relativistic quasiparticles (Fig. 1a). At this point, the MCT 3D Kane fermions[50] exhibit linear dispersion and unconventional collective charge dynamics[51]. In magnetic fields, the strong magneto-optical response and large effective g-factor support electric-dipole-allowed spin-split inter- and intra-LL transitions naturally in the THz range[48,49].

In this work, we experimentally demonstrate a highly non-perturbative light-matter interaction in MCT and establish it as a tunable material platform for THz polaritonics. We use MCT with $x = 0.15$, which hosts Kane fermions with linear dispersion near the critical temperature $T_c \approx 100$ K. As temperature increases, the band gap evolves, and carriers are thermally excited into the conduction band, raising the Fermi level[52–56] (Fig. 1b, c). The combination of ultralight cyclotron masses, intrinsic Fabry-Perot cavity modes, and electron concentrations far exceeding those attainable in quasi-2D III–V quantum-well systems enables Landau polaritons in bulk MCT to enter the deep-strong-coupling regime without the need for subwavelength metasurfaces. Using a multimode microscopic theory and classical electromagnetic simulations to analyse the polariton spectra, we determine the normalised single-mode coupling ratio of >1.6 beyond room temperature. Close to the critical temperature, the normalised single-mode coupling ratio remains close to unity, while the Kane gap E_G closes, causing the conduction-band dispersion $E = (E_G/2) + \sqrt{(E_G/2)^2 + (\hbar v k)^2}$, with k the three-dimensional (3D) wavevector and $v \approx 10^6$ m/s the Kane velocity[50], to become essentially linear near the Fermi level and the band curvature, $\partial^2 E/\partial k^2|_{E_F}$, to vanish (Fig. 1d). This regime therefore provides an ideal platform to test the existence of an effective $\mathbf{A}^2$ term in the low-energy theory and, consequently, the possibility of a superradiant phase transition. We find that a microscopic quantum model based on a consistent low-energy truncation naturally generates an effective $\mathbf{A}^2$ term and accurately reproduces the experimental spectra, thereby strongly supporting the absence of a superradiant phase transition and underscoring the importance of consistent truncation schemes in cavity QED.

Results

Samples and experiment

We investigate MCT/CdTe heterostructures with a $h = 4$ μm-thick molecular beam epitaxial layer of MCT with $x = 0.15$. We fabricate the photonic cavity by bonding the MCT side to a Cu/Au-coated laminate using a dielectric layer (Fig. 2a). By chemical etching, we remove the GaAs substrate, and the resulting structure sustains Fabry-Perot modes in the frequency range where the cyclotron resonances occur. Details of the sample design and fabrication are provided in the Methods Sec. Sample Preparation.

We use the transfer-matrix method to calculate the spatial distributions of the electric field in the sample (Supplementary Information Sec. S2). The model incorporates temperature-dependent 3D conductivity in MCT, and a temperature-dependent harmonic oscillator contribution for the phonon modes. These calculations indicate that, at zero magnetic field and low temperatures (low carrier concentration in the MCT layer), the structure supports two resonances in our spectral range, below 3.5 THz (Fig. 2b). The lowest mode M_1^0, near 1 THz, is a photonic $L = \lambda_1/4 = 22$ μm mode. Such quarter-wave modes form due to asymmetric boundary conditions, with a node at the metal-dielectric interface and an anti-node at the vacuum-CdTe interface. The second mode M_2^0, at about 3 THz, arises from the resonant strong coupling between the $L = 3\lambda_2/4$ FP mode and the MCT phonon mode (Supplementary Information, Sec. S2, Fig. S5a).

The reflectivity of the system as a function of magnetic field B and temperature T is probed experimentally by a commercial THz time-domain spectrometer. Linearly-polarised THz pulses are incident at 8° in the Faraday geometry. The presented frequency-domain spectra show the amplitude of the Fourier transform of time-domain reflection traces, i.e., these are electric field spectra. They are normalised to the reflection spectrum of the metallic mirror holder. Further experimental details are provided in the Methods, Sec. Experimental setup.

Zero magnetic field spectra

In our samples, at low temperatures, MCT has an electron concentration of approximately 2×10^{14} cm^{-3} and a mobility ~10^6 cm^2/Vs (Supplementary Information, Sec. S5). With rising temperature, electron density increases by two orders of magnitude above room temperature (Fig. 1b), as confirmed by complementary Hall effect measurements on a reference sample with the GaAs substrate (see Supplementary Information, Sec. S5 and Fig. S11). Those high carrier densities, compared to quasi-2D semiconductor heterostructures, lead to the deep strong coupling of Landau polaritons, reported further as a function of the magnetic field.

The evolution of electron concentration with temperature also strongly affects the Fabry-Perot resonances at zero magnetic field. Figure 2b presents the temperature evolution of reflection spectra at zero magnetic field (Fig. 2d shows spectra for three selected temperatures). We observe a pronounced resonance, referred to later as M_1, across the entire temperature range, rising to higher frequencies with temperature, from 1 THz at 10 K to 2.3 THz at 370 K. The frequency of M_1 increases due to increasing carrier density in the MCT layer. A similar effect was reported in THz plasmonic cavities based on the narrow-gap semiconductor InSb[57]. As the carrier concentration increases, the MCT layer becomes an increasingly effective screen for electromagnetic waves near 1 THz. As a result, at high temperatures, M_1 is pushed out of the MCT layer, reducing the effective mode length. Above about 100 K, the frequency of M_1 rises more slowly, because further changes in carrier density no longer lead to significant modifications of the effective mode length. This observation is fully consistent with transfer-matrix calculations, which show that at low carrier concentrations, MCT is nearly transparent at M_1 frequency (Fig. 2c, 10 K). The progressive increase of the screening effect can be observed in the field maps for 100 K and 300 K, whereas at 300 K the field is very well localised in the CdTe layer (Fig. 2c, 300 K). As shown below, this screening effect is also fully captured by the microscopic model and is directly related to the $\mathbf{A}^2$ term in the Hamiltonian.

Above 3 THz, the blueshifted M_2 mode exhibits only a weak increase in frequency with temperature (Fig. 2b). This is because the

https://doi.org/10.1038/s41467-026-79076-6

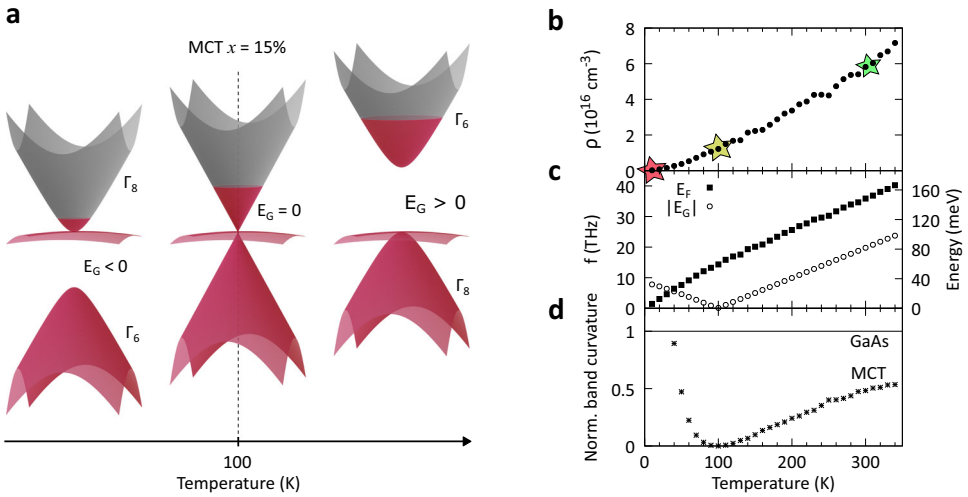


Fig. 1 | Kane fermions in MCT. a Temperature evolution of the electronic band structure from an inverted semimetallic phase ($E_G < 0$) at low temperatures to a normal semiconducting phase ($E_G > 0$) at high temperatures. At the critical temperature $T_c \approx 100$ K (for $x = 0.15$), the band structure becomes gapless. At this point, the bands exhibit linear momentum dispersion and host Kane fermions. With increasing temperature, the Fermi level rises into the conduction band (red indicates occupied states). **b** Temperature dependence of the electron density in MCT; coloured stars mark the temperatures corresponding to the reflection spectra shown in Fig. 2. **c** Temperature dependence of the Fermi energy (E_F) and band gap ($|E_G|$) (both shown in meV and converted to THz). **d** Conduction-band curvature at the Fermi level, $\partial^2 E/\partial k^2|_{E_F}$, normalised to that of GaAs (dashed horizontal line). The vanishing curvature near 100 K indicates an essentially linear Kane-band dispersion.

M_2^0 mode has a small overlap with the MCT layer, as shown by the transfer-matrix calculations in Fig. 2c. This interpretation is further supported by the microscopic model, which shows that the strength of the $\mathbf{A}^2$ term responsible for the blueshift directly depends on the light-matter coupling strength.

Landau levels of bulk Kane fermions

Our description of electrons in the MCT layer is based on the standard Kane model[50], as detailed in Ref. 48. Retaining only the terms linear in the wavevector and neglecting the Γ_7 band, which lies ~1 eV away from the low-energy sector of interest, the model contains three energy bands (Fig. 1a), each doubly degenerate due to time-reversal symmetry. In the presence of a static magnetic field B, electron bands split into non-equidistant LLs dispersing with the wavevector component along the cavity axis (transverse wavevector k_z). In this work, we focus on the conduction band, as the transitions between LLs within the valence band are Pauli-blocked in the studied temperature range. Moreover, transitions from either the valence band or the flat band to the conduction band occur at energies much higher than the cavity modes and therefore contribute only marginally to the spectra. The LL energies in the conduction band read

$$E_{n,k_z,\sigma} = \frac{E_G}{2} + \sqrt{\frac{E_G^2}{4} + \left(\frac{\hbar v}{l_0}\right)^2 \left(2n - 1 + \frac{\sigma}{2}\right) + (\hbar v k_z)^2}, \quad (1)$$

where n is the LL index (a non-negative integer), and $l_0 = \sqrt{\hbar/(eB)}$ is the magnetic length. The quantum number $\sigma = \pm 1$ arises from the breaking of time-reversal symmetry by the applied magnetic field and can be interpreted as the spin projection along the field direction[48]. The LL dispersion along k_z is shown in Fig. 3a for a magnetic field $B = 0.45$ T, in the two sectors $\sigma = \pm 1$ for a fixed electron density at $T = 30$ K obtained by fitting the experimental data with a microscopic model at zero magnetic field, as explained below. Filled states below the Fermi energy E_F lie within the shaded area. Owing to the 3D character of the MCT layer and the non-equidistant LL spectrum, dipole-allowed transitions between the highest occupied level $n = \nu_\sigma(k_z)$ and the lowest empty level $n = \nu_\sigma(k_z) + 1$, with transition energy $\Delta_{k_z,\sigma} = E_{\nu_\sigma+1,k_z,\sigma} - E_{\nu_\sigma,k_z,\sigma}$, acquire a finite dispersion along k_z (Fig. 3b). These cyclotron transitions between consecutive LLs therefore form a quasi-continuous band when all allowed k_z values are considered (shaded regions in Fig. 3b). This behaviour contrasts with the linear B-field dependence of CR frequency eB/m_{GaAs}, observed in GaAs, where equally spaced LLs remain independent of layer thickness owing to the parabolic k_z dispersion. As shown in the next section, however, the collective character of the light-matter coupling in MCT effectively gives rise to a single "bright mode" that couples to the cavity mode. In the low magnetic field limit, $l_0 \gg \hbar/\sqrt{m^* E_F}$, the n-dependence in Eq. (1) becomes negligible, yielding a degenerate CR composed of contributions from many LLs. In this regime, the transition frequency increases linearly with magnetic field, i.e., $\Delta_{k_z,\sigma}/\hbar \sim eB/m^*$, where the **cyclotron** mass of MCT electrons reads $m^* = |E_F - (E_G/2)|/v^2$. This value can be compared to the cyclotron mass $m_{GaAs} = 0.067\, m_0$, of conduction band electrons in gallium arsenide (m_0 is the free-electron mass). The inset of Fig. 3b displays the effective mass ratio. The increase in cyclotron mass is caused by the temperature evolution of the band structure and the rise in Fermi energy. At low temperature ($T \sim 10$ K), the cyclotron mass in MCT is almost two orders of magnitude smaller than the one in GaAs, while at very high temperature it is lower by a factor >3. Such low values for the cyclotron mass are a key factor enabling the large light-matter coupling ratios discussed below.

Deep strong coupling of Kane fermions

Our main results are displayed in Fig. 4a, which shows the magnetic-field dependence of the reflection spectra measured at different temperatures. At 10 K, we observe the CR with an almost linear dependence on magnetic field. Modes M_1^0 and M_2^0 are magnetic-field independent and are indicated by black dashed lines. Raw time-domain traces, as well as data for additional temperatures, are available in the Supplementary Information, Sec. S3.

At elevated temperatures, the increased free-electron concentration enhances the coupling strength Ω_1 between the cyclotron resonance (CR) and the M_1^0 cavity mode. The polarisation degeneracy of the M_1^0 mode in a circular geometry is lifted by its coupling to the CR. The co-rotating component of the cavity field couples strongly to the CR, giving rise to upper and lower co-rotating polaritons (crUP and

https://doi.org/10.1038/s41467-026-79076-6

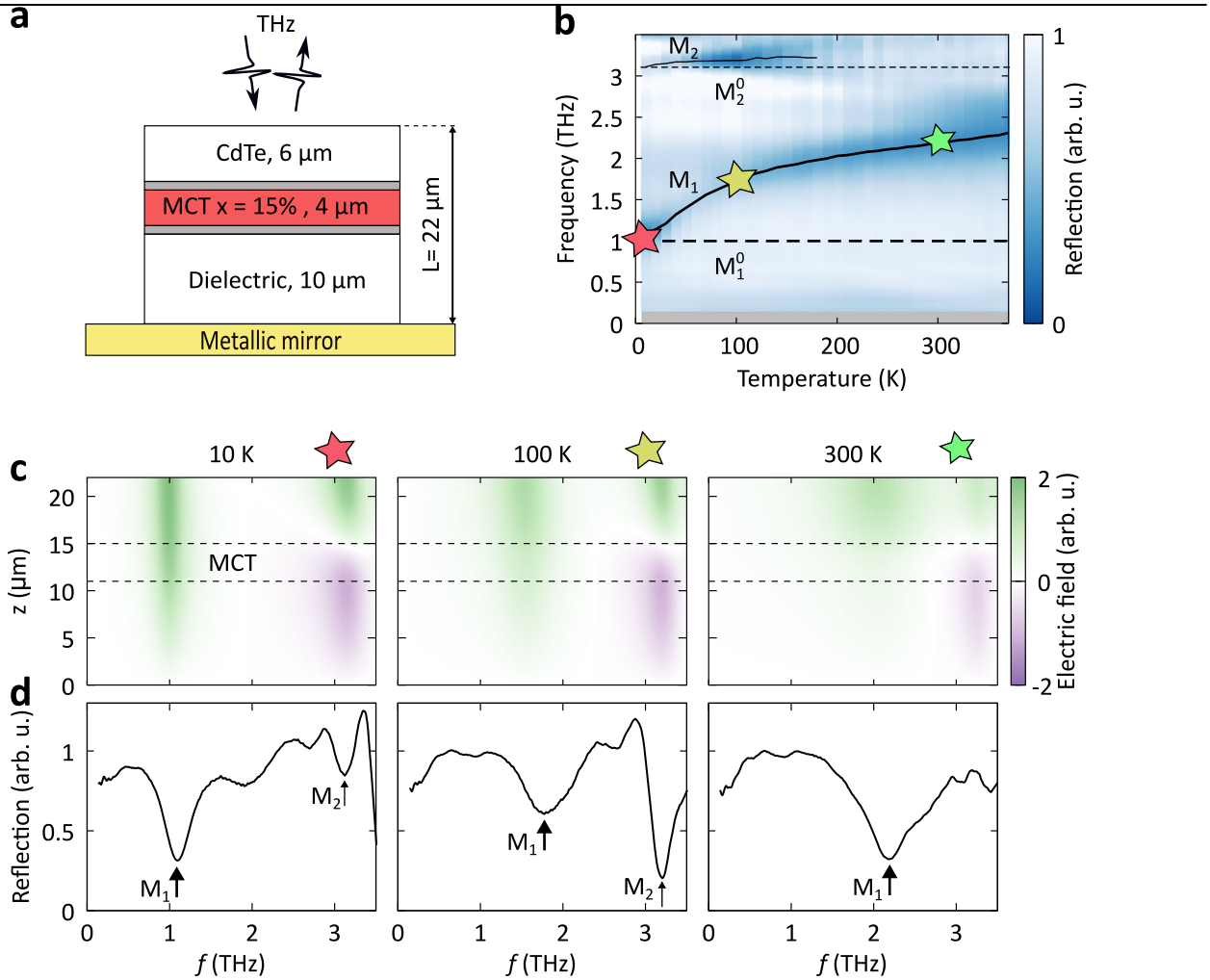


Fig. 2 | Sample and cavity modes. a The heterostructure schematic indicates the active MCT layer as the red block, which is sandwiched by ~1 µm-thick MCT layers with Cd composition continuously graded from 45% to 15% (grey blocks). We probe the sample using THz-TDS in reflection mode. **b** Temperature evolution of M_1 and M_2 modes in reflection spectra (solid lines). M_1^0 and M_2^0 denote the modes in the absence of carriers in the MCT layer (dashed lines). **c** Calculated real part of the electric field profile in the cavity at zero magnetic field and selected temperatures. **d** Reflection spectra at the same selected temperatures. Arrows mark M_1 and M_2 modes.

crLP). In contrast, the anti-rotating component couples weakly, creating the arP branch, which is described in the quantum picture as the vacuum Bloch-Siegert shift[46], or in classical electromagnetism by the negative CR frequency in the MCT dielectric function. Together, these three modes form the characteristic zigzag-shaped Landau-polariton dispersion.

Previous observations with GaAs systems required cavities with narrow linewidths[46]. Here, we observe a very strong effect for high electronic density, even though the polariton resonances are much broader. This qualitatively attests to the highly non-perturbative regime of light-matter interaction observed here. An interesting observation from the data is that, as the magnetic field is increased, the crLP mode asymptotically approaches the unscreened Fabry-Perot mode M_1^0 at 1 THz. This is further confirmed by cavity field maps (Supplementary Information, Sec. 2, Fig. S6).

The CR-M_2^0 interaction strength Ω_2 also increases, although it remains much weaker than the coupling to M_1^0. This is caused by a small overlap of the M_2^0 electric field with the MCT layer. Above 200 K, the high-frequency upper Landau polariton is pushed outside the studied magnetic field range.

We simulate the reflection spectra (Fig. 4b) using the transfer matrix method, assuming normal incidence on the stack of dielectric layers (Fig. 2a). To describe the magneto-optical properties of the MCT layer, we use the gyrotropic dielectric tensor[58]. The transfer matrix method uses the same parameters as the microscopic model described further (Sec. Microscopic quantum model), namely the same carrier density (Fig. 1b) and the CR frequency (Fig. 3b). It incorporates losses and broadening through the imaginary part of the dielectric functions of the layers. Full details of model parameters are provided in the Supplementary Information, Sec. 2. Moreover, we also used the transfer matrix method to compute the electric field distribution in the cavity as a function of the frequency, magnetic field, and temperature. This is important in our system with strong radiation loss, since, as we show in the Supplementary Information (Sec. S2 and Fig. S7), the electric field maxima in the MCT layer do not coincide with the minima observed in reflectivity. Yet, the electric field maxima in the MCT layer match the polariton frequencies inferred from the microscopic quantum model discussed in the next section. The small discrepancy between the polariton eigenenergies predicted by the microscopic model and the classical simulations around 3 THz originates from the phonon mode that is not included in the microscopic model.

Microscopic quantum model

Although the polariton reflection spectra can be fully reproduced by classical simulations, as shown above, a microscopic quantum description provides valuable physical insight into the underlying mechanisms. We therefore developed a microscopic quantum model

https://doi.org/10.1038/s41467-026-79076-6

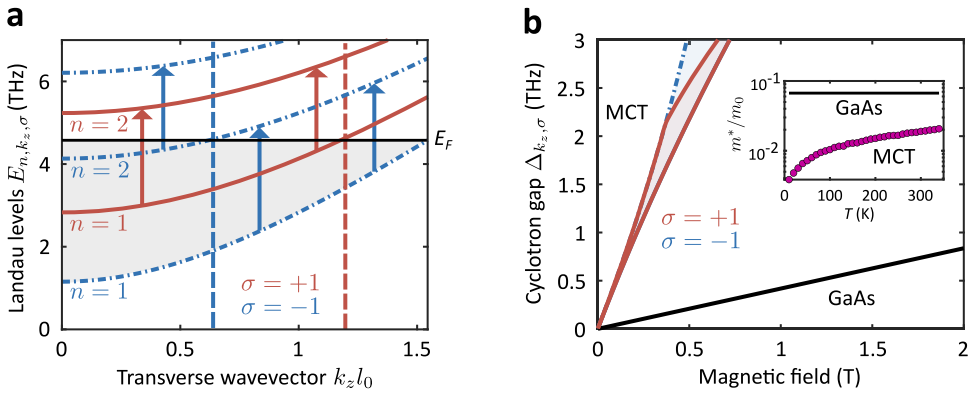


Fig. 3 | LL dispersion and cyclotron transitions in MCT. a Energy dispersion of the conduction-band LL $E_{n,k_z,\sigma}$ at $B = 0.45$ T and $T = 30$ K (electron density $\rho = 1.48 \times 10^{15}$ cm^{-3}). The Fermi energy E_F is shown as a horizontal black line. Filled states lie within the shaded area. Blue (red) curves denote the $\sigma = -1$ ($\sigma = +1$) sector. Dipole-allowed, σ-conserving transitions between the highest occupied and lowest empty LLs are marked by arrows. As k_z moves from left to right across the vertical blue (red) dotted line, the filling factors ν_- (ν_+) decrease from 2 (1) to 1 (0). **b** Cyclotron gap $\Delta_{k_z,\sigma}$ between the last filled and first empty LLs as a function of magnetic field B, forming quasi-continuous bands in the $\sigma = -1$ (blue shaded region) and $\sigma = +1$ (red shaded region) sectors at $T = 30$ K. For comparison, the black line indicates the CR frequency eB/m_{GaAs} of electrons in the conduction band of GaAs, with $m_{\mathrm{GaAs}} = 0.067\, m_0$. Inset: temperature dependence of the cyclotron mass ratio m^*/m_0 for MCT electrons (magenta dots) as compared to m_{GaAs}/m_0 (horizontal line). All energies are converted to THz.

incorporating the first two cavity modes of the open resonator. The bare cavity modes are modelled as the $\lambda_1/4$ (M_1^0) and $3\lambda_2/4$ (M_2^0) resonances. Because the MCT layer thickness $h \simeq 4\,\mu$m is much smaller than the total cavity length $L = 22\,\mu$m, spatial variations of the cavity field along the growth direction are neglected within the active region. The centre of this layer is located at $z_0 = 12\,\mu$m away from the metal-dielectric interface ($z = 0$) and 8 μm away from the dielectric-air interface ($z = L$).

To establish the light-matter interaction Hamiltonian, we start from the model introduced in Ref. 48, originally formulated for $k_z = 0$, and extend it to arbitrary k_z to capture the bulk character of Kane fermions in the MCT layer. The resulting eigenstates are then used to evaluate the photonic pseudopotential, following the procedure outlined in Ref. 59. We find that the coupling between the effective CR in MCT and the two cavity modes M_j^0 with frequencies ω_j ($j = 1,2$) is described by the extended Hopfield Hamiltonian[2] (see Supplementary Information Sec. S1)

$$\hat{H} = \sum_j \hbar\omega_j \left(\hat{a}_{j,l}^\dagger \hat{a}_{j,l} + \hat{a}_{j,r}^\dagger \hat{a}_{j,r}\right) + \sum_{j,j'} \hbar D_{j,j'} \left(\hat{a}_{j,r} + \hat{a}_{j,l}^\dagger\right)\left(\hat{a}_{j',l} + \hat{a}_{j',r}^\dagger\right) + \Delta_{\mathrm{bright}} \hat{l}^\dagger \hat{l} + \sum_j \hbar\Omega_j \left[\left(\hat{l}^\dagger \hat{a}_{j,l} + \hat{l}\hat{a}_{j,l}^\dagger\right) + \left(\hat{l}\hat{a}_{j,r} + \hat{l}^\dagger \hat{a}_{j,r}^\dagger\right)\right], \quad (2)$$

($\hat{a}_{j,r}^\dagger$) creates a left- (right-) circularly polarised in-plane photon in mode M_j^0, corresponding respectively to the co-rotating (anti-rotating) mode with respect to the CR for $B > 0$ (Fig. 5a). The CR operator $\hat{l}^\dagger$ creates a collective "bright mode", a coherent superposition of dipolar excitations from the highest occupied LL to the lowest empty one,

$$\hat{l}^\dagger = \frac{1}{\sqrt{\bar{\nu}N}} \sum_{k_x,k_z,\sigma} \hat{c}_{\nu_\sigma+1,k_x,k_z,\sigma}^\dagger \hat{c}_{\nu_\sigma,k_x,k_z,\sigma},$$

where $\hat{c}$ and $\hat{c}^\dagger$ are the annihilation and creation electron operators. The operators l and $l^\dagger$ are quasi-bosonic in the low excitation limit[32]. Here, k_x is the guiding centre of the cyclotron orbit in the x-direction[60], N is the LL degeneracy, and $\bar{\nu} = \sum_{k_z,\sigma} \nu_\sigma(k_z)\, \xi_{\nu_\sigma,k_z,\sigma}$ is an effective filling factor, with $\xi_{\nu_\sigma,k_z,\sigma}$ a dimensionless overlap factor between LL wavefunctions defined in the Supplementary Information Sec. S1.

The bright-mode energy is defined as $\Delta_{\mathrm{bright}} = \frac{1}{2\mathcal{N}} \sum_{k_z,\sigma} \Delta_{k_z,\sigma}$, corresponding to the average of the cyclotron gaps over all k_z and spin indices σ, with $\mathcal{N}$ denoting the number of k_z values. As illustrated in Fig. 5b, the polariton frequencies obtained from the diagonalization of the full Hamiltonian (black markers, see Supplementary Information Sec. S1), which incorporates all possible cyclotron transitions with energies $\Delta_{k_z,\sigma}$ (shaded regions in Fig. 3b), are numerically indistinguishable from those derived from the effective model in Eq. (2) (blue curves; also shown as thin black lines in Fig. 4a, b). Thus, despite the strong frequency spread of the cyclotron gaps shown in Fig. 3b, the polariton eigenfrequencies of the full Hamiltonian all lie within the values predicted by the effective Hamiltonian (2), with a single bright mode concentrating all the oscillator strength. The bright mode co-rotates with the cyclotron motion and, as apparent from Eq. (2), couples resonantly to left-circularly polarised photons. At the same time, the coupling to right-circular polarisation arises only from anti-rotating terms[46], yielding a strong vacuum Bloch-Siegert shift in our data. Besides the bright mode, the full Hamiltonian predicts a large number of dark modes whose energies remain close to those of the bare cyclotron transitions and which are only weakly coupled to the cavity field. We believe that these dark modes could lead to nonlocal effects for resonators featuring strong spatial inhomogeneity of the electric field[29]. The emergence of a single bright mode provides a microscopic justification for the gyrotropic dielectric tensor used in the transfer-matrix calculations.

The light-matter coupling frequency strength reads

$$\Omega_j = \frac{\Delta_{\mathrm{bright}}}{\hbar} \sin\left[\frac{(2j-1)\pi z_0}{2L}\right] \sqrt{\frac{4\alpha\,\bar{\nu}}{\pi(2j-1)\sqrt{\epsilon}}}, \quad (3)$$

with $\epsilon \simeq 13.7$ the background dielectric constant of the MCT layer, $\alpha \simeq 1/137$ the fine-structure constant. The key parameter controlling the light-matter interaction is the effective filling factor $\bar{\nu}$. In the low-field limit, $l_0 \gg \hbar/\sqrt{m^* E_F}$, state counting yields $\bar{\nu} \simeq 2\pi l_0^2 \rho h$, such that $\Omega_j \propto \sqrt{\rho h}$, reflecting the cooperative nature of the coupling[28,32]. This scaling further implies that thicker MCT layers can sustain stronger interactions, provided the cavity field remains approximately uniform across the active region. The excellent agreement between transfer-matrix calculations, which fully capture the field profile, and the microscopic quantum model confirms that this condition is well satisfied in the present structures. At the resonant field B_{res}^j, defined by $\Delta_{\mathrm{bright}} \simeq \hbar e B_{\mathrm{res}}^j/m^* = \hbar\omega_j$, the effective filling factor becomes $\bar{\nu} \simeq 2\pi\hbar\rho h/(m^*\omega_j)$. The ultralow cyclotron mass of MCT electrons therefore enables substantially larger resonant coupling strengths than in conventional GaAs quantum wells (Fig. 3b). The carrier density

https://doi.org/10.1038/s41467-026-79076-6

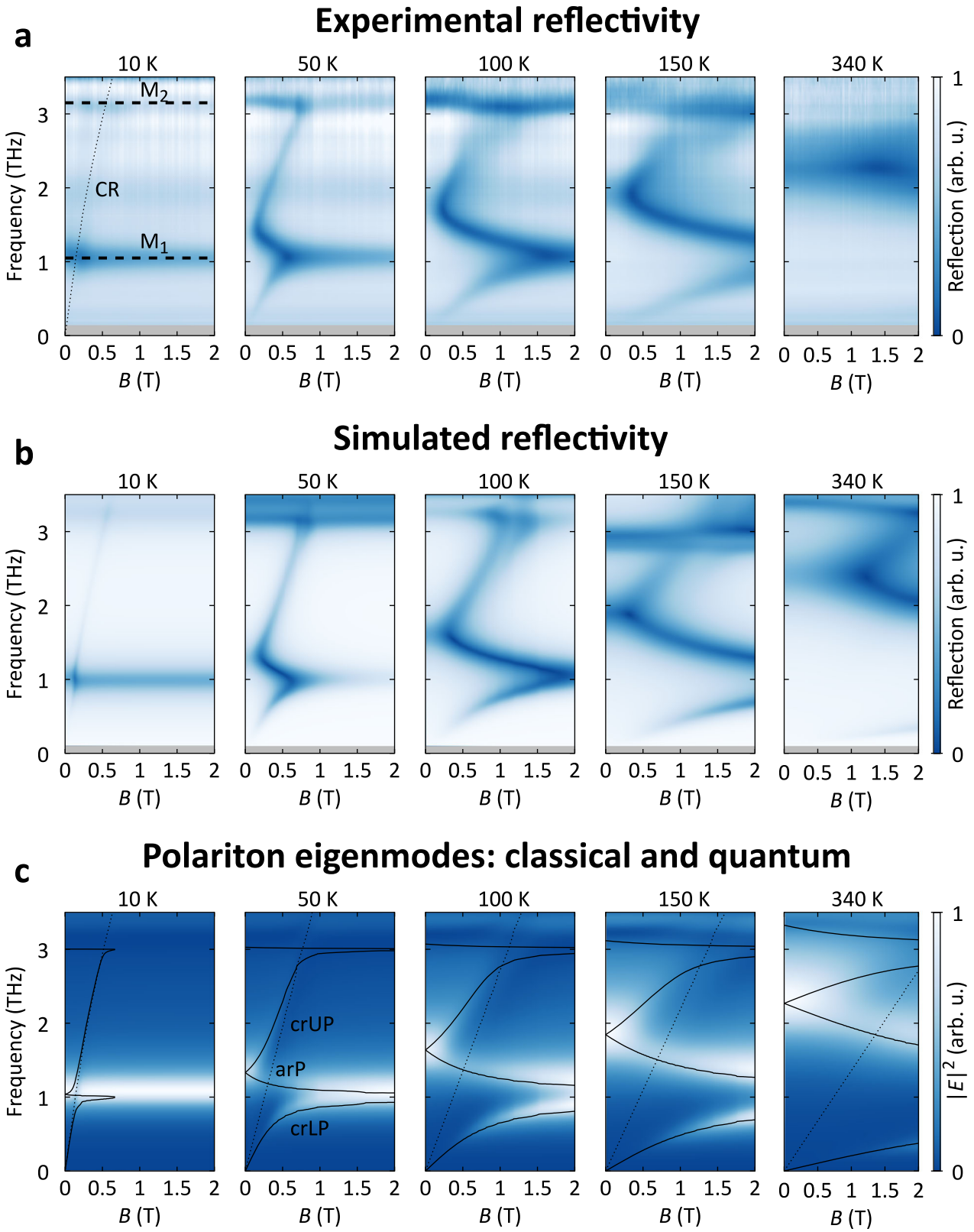


Fig. 4 | Reflection spectra. a Reflection as a function of magnetic field at selected temperatures. Dotted lines indicate the CR. At 10 K, two horizontal dashed lines mark photonic modes M_1^0 and M_2^0. **b** Simulated spectra based on the transfer-matrix model. **c** Comparison between polariton eigenmodes obtained from the transfer-matrix model (energy density in the MCT layer) and the microscopic quantum model. Continuous black lines are eigenvalues of Eq. (2), which are labelled in the 50 K segment---the upper and lower co-rotating polaritons as crUP and crLP, respectively, and the anti-rotating polariton as arP.

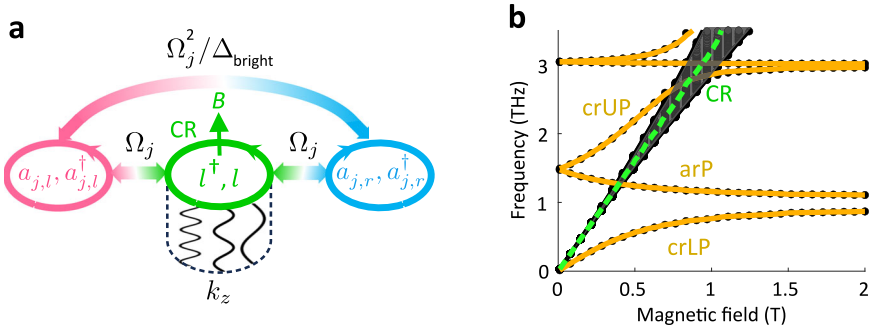


Fig. 5 | Microscopic modelling of MCT polaritons. a Schematic representation of the Hamiltonian (2). The CR collective "bright" mode arises as a coherent superposition of transitions from the highest occupied LL to the lowest unoccupied level, contributed by many transverse wavevectors k_z. This mode couples resonantly to the co-rotating photon modes M_j^0 ($j = 1, 2$) with strength Ω_j, described by the operators $\hat{a}_{j,l}$ and $\hat{a}_{j,l}^\dagger$, and couples antiresonantly to anti-rotating modes associated with $\hat{a}_{j,r}$ and $\hat{a}_{j,r}^\dagger$. The Hamiltonian further incorporates a diamagnetic $\mathbf{A}^2$ term, which renormalises the bare mode frequencies ω_j and induces coupling between left- and right-circular polarisations. **b** Polaritonic eigenmodes of the full Hamiltonian at 90 K, in which each cyclotron transition with frequency $\Delta_{k_z,\sigma}$ (shaded area) is coupled to the cavity modes (black markers), compared with those of the effective Hamiltonian [Eq. (2)] (orange lines). In the effective description, only the collective "bright" mode, with frequency Δ_{bright} (green dashed line), interacts with the cavity modes.

ρ constitutes the only free parameter of the microscopic model. It is determined by fitting the $B = 0$ data, namely by matching the M_1 resonance computed from the microscopic model to the experimentally observed reflectance minima. The same value for the density is used for transfer matrix simulations (Fig. 4b), which provide excellent agreement with the experimental data. Importantly, accounting for the finite thickness of the MCT layer is essential, implying that the out-of-plane momenta $k_z \propto 1/h$ must be treated as a discrete variable in the quantum model. The microscopic model also explains the blueshift of the cavity modes with temperature (Fig. 2b), which originates from the diamagnetic $\mathbf{A}^2$ term in Eq. (2). In the low-field limit, $D_{j,j'} \propto \rho$ remains finite and independent of the magnetic field, whereas the light-matter coupling vanishes as $\Omega_j \propto \sqrt{B}$. This behaviour corresponds to the screening effect visible in the cavity-field profiles of Fig. 2c. Conversely, as the magnetic field increases, the effect of the $\mathbf{A}^2$ term is progressively compensated by the light-matter coupling, and the polariton frequencies asymptotically approach the bare cavity resonances M_j^0.

We now determine the normalised single-mode coupling strengths, Ω_j/ω_j, evaluated at resonance, i.e., at the magnetic field B_{res}^j for which $\Delta_{\text{bright}} = \hbar\omega_j$. Their temperature dependence is shown in Fig. 6a. This quantity is the standard figure of merit used to characterise the ultrastrong and deep-strong coupling regimes.

We find that at 100 K, where the low-energy dispersion becomes linear, the system already exhibits a large coupling strength with a figure of merit $\Omega_1/\omega_1 \approx 1$. At room temperature, this ratio further increases to $\Omega_1/\omega_1 \approx 1.6$, placing the system firmly in the deep-strong-coupling regime. Moreover, even the second cavity mode at $\omega_2/(2\pi) = 3$ THz achieves $\Omega_2/\omega_2 \gtrsim 0.2$, which lies well within the ultrastrong-coupling regime. Another key figure of merit in these extreme light-matter interaction regimes is the emergence of anomalous correlations in the polaritonic ground state[3,45,61], which are a genuine quantum feature of the system. As shown in Fig. 6b, we identify three correlations that acquire the most significant amplitudes: $\langle \hat{a}_{1,l}^\dagger \hat{a}_{1,l} \rangle$ and $\langle \hat{a}_{1,r}^\dagger \hat{a}_{1,r} \rangle$, corresponding to the populations of left- and right-circularly polarised photons, respectively, and $\langle \hat{a}_{1,l}^\dagger \hat{a}_{1,r}^\dagger \rangle$ (together with its complex conjugate), which describes photon pairs with opposite circular polarisations. The latter originates from the diamagnetic term in the Hamiltonian Eq. (2), which induces the antiresonant coupling between left- and right-circular polarisations, and provides a clear signature of strong squeezing in the polaritonic ground state[3]. The order-unity values reported in Fig. 6b are remarkable for a single-mode system and constitute further evidence of the deep-strong-coupling regime.

While larger normalised coupling strengths have been reported in multimode systems[62,63], the corresponding values are extracted from an effective single-mode description of the underlying multimode Hamiltonian and therefore do not represent true single-mode coupling strengths. By contrast, the coupling strengths reported here are directly associated with individual cavity modes.

No-go theorem for Kane fermions

Finally, our work settles the long-standing controversy regarding the possible existence of the Dicke-like superradiant phase transition for materials hosting Dirac-like fermions coupled to a cavity field.

More than a decade ago, it was pointed out that the light-matter Hamiltonian for Dirac fermions in graphene does not contain any $\mathbf{A}^2$ term when the minimal substitution $\mathbf{p} \to (\mathbf{p} - e\mathbf{A})$ is applied directly to the low-energy Dirac Hamiltonian, which is linear in momentum[26]. This has led the authors of Ref. 26 to the conclusion that graphene coupled to a cavity could therefore exhibit a superradiant phase transition when brought to the ultrastrong coupling regime. Subsequently, however, it was pointed out that the low-energy Dirac description necessarily involves an ultraviolet cutoff, which breaks gauge invariance, and that a dynamically generated $\mathbf{A}^2$ term prevents the phase transition from occurring[27].

More generally, it has been emphasised that a direct projection of the minimal-coupling Hamiltonian onto a low-energy subspace can lead to a breakdown of gauge invariance[27,64,65], which is precisely the procedure employed in Ref. 26. Applying a similar approach to the Kane model considered here, whose low-energy Hamiltonian also exhibits a linear momentum dependence near $T \approx 100$ K, yields an effective theory in which the $\mathbf{A}^2$ contribution is absent. Setting $D_{j,j'} = 0$ in Eq. (2) and neglecting the high-frequency cavity mode M_2^0, the Hamiltonian reduces to a generalised Dicke model with two degenerate polarisations. In the absence of thermal fluctuations, this model exhibits a critical point at $\Omega_1^c = \sqrt{\Delta_{\text{bright}}\,\omega_1/(2\hbar)}$ corresponding to the softening of the lower polariton branch to zero frequency. For $\Omega_1 > \Omega_1^c$, the system enters a superradiant phase characterised by a macroscopic occupation of the cavity mode and a macroscopic polarisation across the LLs. Using Eq. (3), the magnetic field drops out of the criticality condition, yielding a critical carrier density

$$\rho_c = \frac{(2j-1)\sqrt{\epsilon}}{h \sin\left[(2j-1)\pi z_0/(2L)\right]} \frac{m^* \omega_1}{16\hbar\alpha} \simeq 5.6 \times 10^{15}\ \text{cm}^{-3}. \tag{4}$$

At $T = 100$ K, the fitted carrier density is $\rho \simeq 1.2 \times 10^{16}\ \text{cm}^{-3} > \rho_c$, implying that the system should already be in the superradiant phase

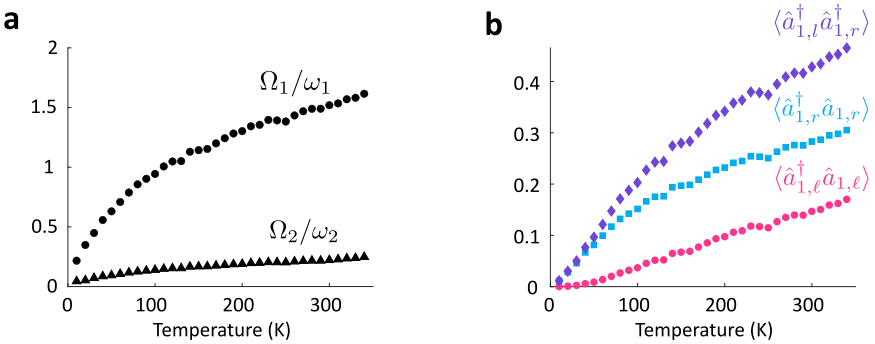


Fig. 6 | Deep strong coupling figures of merit for MCT Landau polaritons. **a** Temperature dependence of the normalised coupling strength Ω_j/ω_j for the photon modes M_j^0 ($j = 1, 2$). **b** Ground-state photon populations in the first cavity mode M_1^0, for left- (pink) and right- (blue) circular polarisations, $\langle a^\dagger_{1,p}a_{1,p}\rangle$ ($p = l, r$), together with the inter-polarisation correlations $|\langle a^\dagger_{1,l}a^\dagger_{1,r}\rangle|$. Here $\langle \cdots \rangle$ denotes the expectation value evaluated in the ground state of the Hamiltonian Eq. (2).

according to the Dicke model. Such a scenario is incompatible with the experimental observations: no qualitative change is observed in the polariton spectrum upon crossing the temperature at which the dispersion becomes linear. Instead, the spectra remain accurately described at all temperatures by our Hopfield-like model containing an effective $\mathbf{A}^2$ term.

To derive this Hamiltonian, we followed the procedure proposed in Refs. 59,66,67, which preserves gauge invariance by first projecting the fermionic fields onto the low-energy sector and subsequently deriving the light-matter interaction through a consistently projected unitary transformation. Moreover, the Hamiltonian (2) is formally identical to that used to describe a GaAs quantum well with quadratic dispersion coupled to a THz cavity with Bragg mirrors[46]. In the single-mode, single-polarisation limit, it also reduces exactly to the Hamiltonian derived in Ref. 27 for graphene coupled to a cavity mode.

We therefore conclude that low-energy truncation schemes that consistently preserve gauge invariance yield effective cavity-QED Hamiltonians for Kane fermions that are fully compatible with the experimental observations and strongly support the absence of a superradiant phase transition in non-perturbative regimes of light-matter coupling.

Discussion

We have realised Landau polaritons using the bulk $Hg_{0.85}Cd_{0.15}Te$ layer in the Fabry-Perot cavity and accessed the deep-strong-coupling regime with Kane fermions. Normalised single-mode coupling ratio reached $\Omega/\omega = 1.6$ above room temperature through thermal excitation of carriers. The temperature evolution of the spectra further reveals how electronic screening reshapes the cavity field and controls the polaritonic response, while the magnetic field provides an additional tuning parameter. Unlike previous platforms relying on local field enhancement in subwavelength metamaterial resonators[28,34,38], the present architecture exploits the bulk nature of the active medium, enabling a cooperative enhancement of the light-matter interaction with increasing layer thickness. Combined with the ultralow cyclotron mass of MCT carriers, this offers a direct route towards even stronger coupling regimes.

To describe polaritons formed from 3D Kane fermions, we developed a gauge-invariant microscopic theory fully accounting for their relativistic energy dispersion. This framework encompasses previous models based on parabolic bands[32,46] and extends naturally to 2D relativistic systems such as graphene[68]. The quantitative agreement between experiment and theory provides strong support for the no-go scenario in a Kane-fermion platform. Our microscopic description in terms of a single bright mode also agrees well with transfer-matrix simulations describing the optical response in terms of an effective dielectric tensor.

Beyond the present realisation, the Fabry-Perot geometry offers a versatile platform to explore multipartite deep-strong-coupling systems, including hybridisation with disparate quasiparticles, such as magnons[69]. Carrier populations could also be controlled optically rather than thermally, enabling low-temperature operation and time-resolved studies of polariton dynamics with ultrafast THz spectroscopy[34,70]. The same geometry may provide access to quantum vacuum fluctuations through THz electro-optical detection[71,72], offering a possible route to probe the large and unusual quantum correlations predicted here (Fig. 6b). More generally, combining this architecture with transport-compatible heterostructures may open opportunities to study electronic transport in the deep-strong-coupling regime[15,36,39], as well as for tunable cavity-coupled THz detector and emitter[33] architectures.

Methods

Sample preparation

A bulk MCT crystal is grown by molecular beam epitaxy on a GaAs substrate. The substrate is removed by wet etching in a H_2O_2/NH_4OH solution, yielding a free-standing flake with lateral dimensions of 5×5 mm. The resulting stack consists of three main layers: 10 µm of epoxy glue, 4 µm of $Hg_{0.85}Cd_{0.15}Te$, and a 6 µm CdTe buffer layer (Fig. 1a). The central $Hg_{0.85}Cd_{0.15}Te$ region is symmetrically enclosed by ~1 µm-thick graded $Hg_{1-x}Cd_xTe$ layers, in which the Cd content varies monotonically from 45% to 15%. Exemplary scanning electron microscopy images of the studied sample are provided in Ref. 73 and Supplementary Information.

Experimental setup

The samples are mounted at the centre of a 2 T superconducting magnet and cooled in darkness to 10 K. We measure reflection time-domain traces in the Faraday geometry as a function of magnetic field B (20 mT steps) and temperature T (10 K steps). Measurements are performed using a TeraFlash pro time-domain spectrometer (*TOPTICA Photonics*) based on photoconductive antenna emitter-detector pairs, driven by a laser centred at 1560 nm, which produces 80 fs pulses with 80 MHz repetition rate. Two antenna sets (centred at 0.5 and 1 THz) provide a spectral bandwidth of 0.14–3.5 THz with a 5 GHz resolution (200 ps scan window) and a signal-to-noise ratio exceeding 120 dB. The THz beam is directed onto the samples at an incidence angle of 8° using off-axis parabolic mirrors. The THz path outside of the cryostat is continuously purged with dry nitrogen.

Transfer matrix model

We employ the transfer-matrix formalism[74] to quantitatively describe the magneto-optical response of the full heterostructure, including the metallic holder. We consider an electromagnetic plane THz wave incident normally from vacuum. The stack of layers ends with a semi-

infinite metallic copper substrate. Material parameters used in the modelling are provided in the Supplementary Information Sec. S2.

Microscopic model

The light-matter coupling is described using a gauge-invariant microscopic quantum model based on the low-energy Kane Hamiltonian for MCT fermions in a magnetic field, extended to finite k_z to account for the bulk character of the electronic states. The first two open Fabry-Perot cavity modes are quantised and coupled to LL transitions through a projected minimal-coupling Hamiltonian derived via a unitary gauge transformation depending on the LL wavefunctions. In the low-excitation regime, the electronic (dipolar) transitions are mapped onto collective bosonic magneto-exciton operators, yielding an effective bright mode concentrating the oscillator strength of the continuum of cyclotron transitions. Spin-flip excitations are shown to contribute negligibly to the collective coupling and are neglected. The resulting Hopfield-like Hamiltonian is diagonalised to obtain the polariton eigenmodes and ground-state correlations used to model the experimental spectra.

Data availability

The data generated in this study have been deposited in the Zenodo database under accession code https://doi.org/10.5281/zenodo.22115449.

Code availability

The code used in this study is available from the corresponding authors upon request.

References

1. Kimble, H. J. Strong interactions of single atoms and photons in cavity QED. *Phys. Scr.* **T76**, 127 https://doi.org/10.1238/Physica.Topical.076a00127 (1998).
2. Hopfield, J. J. Theory of the contribution of excitons to the complex dielectric constant of crystals. *Phys. Rev.* **112**, 1555–1567 https://doi.org/10.1103/PhysRev.112.1555 (1958).
3. Ciuti, C., Bastard, G. & Carusotto, I. Quantum vacuum properties of the intersubband cavity polariton field. *Phys. Rev. B* **72**, 115303 https://doi.org/10.1103/PhysRevB.72.115303 (2005).
4. Kockum, A. F., Miranowicz, A., Liberato, S. D., Savasta, S. & Nori, F. Ultrastrong coupling between light and matter. *Nat. Rev. Phys.* **1**, 19–40 https://doi.org/10.1038/s42254-018-0006-2 (2019).
5. Forn-Díaz, P., Lamata, L., Rico, E., Kono, J. & Solano, E. Ultrastrong coupling regimes of light-matter interaction. *Rev. Mod. Phys.* **91**, 025005 https://doi.org/10.1103/RevModPhys.91.025005 (2019).
6. Garcia-Vidal, F. J., Ciuti, C. & Ebbesen, T. W. Manipulating matter by strong coupling to vacuum fields. *Science* **373**, eabd0336 https://doi.org/10.1126/science.abd0336 (2021).
7. Bloch, J., Cavalleri, A., Galitski, V., Hafezi, M. & Rubio, A. Strongly correlated electron-photon systems. *Nature* **606**, 41–48 https://doi.org/10.1038/s41586-022-04726-w (2022).
8. Bretscher, H. M. et al. Fluctuation engineering in cavity quantum materials. Preprint at *arXiv* https://doi.org/10.48550/arXiv.2604.08666 (2026).
9. Jarc, G. et al. Cavity-mediated thermal control of metal-to-insulator transition in 1t-tas$_2$. *Nature* **622**, 487–492 https://doi.org/10.1038/s41586-023-06596-2 (2023).
10. Xu, H. et al. Vacuum-dressed superconductivity in nbn observed in a high-q terahertz cavity. *arXiv:2601.08191* https://arxiv.org/abs/2601.08191 (2026).
11. Keren, I. et al. Cavity-altered superconductivity. *Nature* **650**, 864–868 https://doi.org/10.1038/s41586-025-10062-6 (2026).
12. Hutchison, J. A., Schwartz, T., Genet, C., Devaux, E. & Ebbesen, T. W. Modifying chemical landscapes by coupling to vacuum fields. *Angew. Chem. Int. Ed.* **51**, 1592–1596 https://doi.org/10.1002/anie.201107033 (2012).
13. Thomas, A. et al. Tilting a ground-state reactivity landscape by vibrational strong coupling. *Science* **363**, 615–619 https://doi.org/10.1126/science.aau7742 (2019).
14. Orgiu, E. et al. Conductivity in organic semiconductors hybridized with the vacuum field. *Nat. Mater.* **14**, 1123–1129 (2015).
15. Appugliese, F. et al. Breakdown of topological protection by cavity vacuum fields in the integer quantum Hall effect. *Science* **375**, 1030–1034 https://doi.org/10.1126/science.abl5818 (2022).
16. Andrew, P. & Barnes, W. L. Förster energy transfer in an optical microcavity. *Science* **290**, 785–788 https://doi.org/10.1126/science.290.5492.785 (2000).
17. Zhong, X. et al. Energy transfer between spatially separated entangled molecules. *Angew. Chem. Int. Ed.* **56**, 9034–9038 https://doi.org/10.1002/anie.201703539 (2017).
18. Dicke, R. H. Coherence in spontaneous radiation processes. *Phys. Rev.* **93**, 99–110 https://doi.org/10.1103/PhysRev.93.99 (1954).
19. Hepp, K. & Lieb, E. H. On the superradiant phase transition for molecules in a quantized radiation field: the Dicke maser model. *Ann. Phys.* **76**, 360–404 https://doi.org/10.1016/0003-4916(73)90039-0 (1973).
20. Emary, C. & Brandes, T. Quantum chaos triggered by precursors of a quantum phase transition: the Dicke model. *Phys. Rev. Lett.* **90**, 044101 https://doi.org/10.1103/PhysRevLett.90.044101 (2003).
21. Andolina, G. M., Pellegrino, F. M. D., Giovannetti, V., MacDonald, A. H. & Polini, M. Theory of photon condensation in a spatially varying electromagnetic field. *Phys. Rev. B* **102**, 125137 https://doi.org/10.1103/PhysRevB.102.125137 (2020).
22. Guerci, D., Simon, P. & Mora, C. Superradiant phase transition in electronic systems and emergent topological phases. *Phys. Rev. Lett.* **125**, 257604 https://doi.org/10.1103/PhysRevLett.125.257604 (2020).
23. Rzażewski, K., Wódkiewicz, K. & Żakowicz, W. Phase transitions, two-level atoms, and the A^2 term. *Phys. Rev. Lett.* **35**, 432–434 https://doi.org/10.1103/PhysRevLett.35.432 (1975).
24. Nataf, P. & Ciuti, C. No-go theorem for superradiant quantum phase transitions in cavity QED and counter-example in circuit QED. *Nat. Commun.* **1**, 72 https://doi.org/10.1038/ncomms1070 (2010).
25. Andolina, G. M., Pellegrino, F. M. D., Giovannetti, V., MacDonald, A. H. & Polini, M. Cavity quantum electrodynamics of strongly correlated electron systems: a no-go theorem for photon condensation. *Phys. Rev. B* **100**, 121109(R) https://doi.org/10.1103/PhysRevB.100.121109 (2019).
26. Hagenmüller, D. & Ciuti, C. Cavity qed of the graphene cyclotron transition. *Phys. Rev. Lett.* **109**, 267403 https://doi.org/10.1103/PhysRevLett.109.267403 (2012).
27. Chirolli, L., Polini, M., Giovannetti, V., MacDonald, A. H. & Guinea, F. Drude weight, cyclotron resonance, and the Dicke model of graphene cavity QED. *Phys. Rev. Lett.* **109**, 267404 https://doi.org/10.1103/PhysRevLett.109.267404 (2012).
28. Scalari, G. et al. Ultrastrong coupling of the cyclotron transition of a 2d electron gas to a THz metamaterial. *Science* **335**, 1323–1326 https://doi.org/10.1126/science.1216022 (2012).
29. Rajabali, S. et al. Polaritonic nonlocality in light–matter interaction. *Nat. Photonics* **15**, 690–695 https://doi.org/10.1038/s41566-021-00854-3 (2021).
30. Rajabali, S. et al. An ultrastrongly coupled single terahertz metaatom. *Nat. Commun.* **13**, 2528 https://doi.org/10.1038/s41467-022-30197-1 (2022).
31. Hale, L. L. et al. Cavity modification of magnetoplasmon mode through coupling with intersubband polaritons. Preprint at *arXiv* https://doi.org/10.48550/arXiv.2510.18665 (2025).
32. Hagenmüller, D., De Liberato, S. & Ciuti, C. Ultrastrong coupling between a cavity resonator and the cyclotron transition of a two-

dimensional electron gas in the case of an integer filling factor. *Phys. Rev. B* **81**, 235303 https://doi.org/10.1103/PhysRevB.81.235303 (2010).
33. Benhamou-Bui, B. et al. Nonlinear terahertz electroluminescence from Dirac-Landau polaritons. *Phys. Rev. Lett.* **136**, 096902 https://doi.org/10.1103/7rcf-fd3g (2026).
34. Mornhinweg, J. et al. Tailored subcycle nonlinearities of ultrastrong light-matter coupling. *Phys. Rev. Lett.* **126**, 177404 https://doi.org/10.1103/PhysRevLett.126.177404 (2021).
35. Bartolo, N. & Ciuti, C. Vacuum-dressed cavity magnetotransport of a two-dimensional electron gas. *Phys. Rev. B* **98**, 205301 https://doi.org/10.1103/PhysRevB.98.205301 (2018).
36. Paravicini-Bagliani, G. L. et al. Magneto-transport controlled by Landau polariton states. *Nat. Phys.* **15**, 186–190 https://doi.org/10.1038/s41567-018-0346-y (2019).
37. Ciuti, C. Cavity-mediated electron hopping in disordered quantum Hall systems. *Phys. Rev. B* **104**, 155307 https://doi.org/10.1103/PhysRevB.104.155307 (2021).
38. Appugliese, F. et al. Breakdown of the topological protection by cavity vacuum fields in the integer quantum Hall effect. *Science* **375**, 1030–1034 https://doi.org/10.1126/science.abl5818 (2022).
39. Enkner, J. et al. Tunable vacuum-field control of fractional and integer quantum Hall phases. *Nature* **641**, 884–889 https://doi.org/10.1038/s41586-025-08894-3 (2025).
40. Bacciconi, Z., Xavier, H. B., Carusotto, I., Chanda, T. & Dalmonte, M. Theory of fractional quantum Hall liquids coupled to quantum light and emergent graviton-polaritons. *Phys. Rev. X* **15**, 021027 https://doi.org/10.1103/PhysRevX.15.021027 (2025).
41. Bayer, A. et al. Terahertz light-matter interaction beyond unity coupling strength. *Nano Lett.* **17**, 6340–6344 https://doi.org/10.1021/acs.nanolett.7b03103 (2017).
42. Baydin, A. et al. Terahertz cavity phonon polaritons in lead telluride in the deep-strong coupling regime. Preprint at *arXiv* https://doi.org/10.48550/arXiv.2501.10856 (2025).
43. Mavrona, E. et al. Thz ultrastrong coupling in an engineered fabry–perot cavity. *ACS Photonics* **8**, 2692–2698 https://doi.org/10.1021/acsphotonics.1c00717 (2021).
44. Zhang, Q. et al. Collective non-perturbative coupling of 2d electrons with high-quality-factor terahertz cavity photons. *Nat. Phys.* **12**, 1005–1011 https://doi.org/10.1038/nphys3850 (2016).
45. Tay, F. et al. Multimode ultrastrong coupling in three-dimensional photonic-crystal cavities. *Nat. Commun.* **16**, 3603 https://doi.org/10.1038/s41467-025-58835-x (2025).
46. Li, X. et al. Vacuum bloch–siegert shift in landau polaritons with ultra-high cooperativity. *Nat. Photonics* **12**, 324–329 https://doi.org/10.1038/s41566-018-0153-0 (2018).
47. Zawadzki, W. Electron transport phenomena in small-gap semiconductors. *Adv. Phys.* **23**, 435–522 https://doi.org/10.1080/00018737400101371 (1974).
48. Orlita, M. et al. Observation of three-dimensional massless Kane fermions in a zinc-blende crystal. *Nat. Phys.* **10**, 233 https://doi.org/10.1038/nphys2857 (2014).
49. Teppe, F. et al. Temperature-driven massless Kane fermions in HgCdTe crystals. *Nat. Commun.* **7**, 1 https://doi.org/10.1038/ncomms12576 (2016).
50. Kane, E. O. Band structure of indium antimonide. *J. Phys. Chem. Solids* **1**, 249 https://doi.org/10.1016/0022-3697(57)90013-6 (1957).
51. Charnukha, A. et al. Ultrafast nonlocal collective dynamics of Kane plasmon-polaritons in a narrow-gap semiconductor. *Sci. Adv.* **5**, eaau9956 https://doi.org/10.1126/sciadv.aau9956 (2019).
52. Nemirovsky, Y. & Finkman, E. Intrinsic carrier concentration of $Hg_{1-x}Cd_xTe$. *J. Appl. Phys.* **50**, 8107–8111 https://doi.org/10.1063/1.325950 (1979).
53. Hansen, G. L. & Schmit, J. L. Calculation of intrinsic carrier concentration in $Hg_{1-x}Cd_xTe$. *J. Appl. Phys.* **54**, 1639–1640 https://doi.org/10.1063/1.332153 (1983).
54. Hansen, G. L., Schmit, J. L. & Casselman, T. N. Intrinsic carrier concentrations in long-wavelength HgCdTe based on the new, nonlinear temperature dependence of $E_g(x, T)$. **216**, 59–63 https://doi.org/10.1557/PROC-216-59 (1990).
55. Moldavskaya, M. D. et al. Magnetophotogalvanic effects driven by terahertz radiation in cdhgte crystals with Kane fermions. *Phys. Rev. B* https://doi.org/10.1103/PhysRevB.110.205204 (2024).
56. Yahniuk, I. et al. Positive terahertz photoconductivity in cdhgte under hydrostatic pressure. *Phys. Rev. B* **112**, 075417 https://doi.org/10.1103/hfn6-v2y6 (2025).
57. Aupiais, I. et al. Ultrasmall and tunable terahertz surface plasmon cavities at the ultimate plasmonic limit. *Nat. Commun.* **14**, 7645 https://doi.org/10.1038/s41467-023-43394-w (2023).
58. Miura, N. 2.08 - magneto-spectroscopy of semiconductors. In Bhattacharya, P., Fornari, R. & Kamimura, H. (eds.) *Comprehensive Semiconductor Science and Technology*, 256–342 https://www.sciencedirect.com/science/article/pii/B9780444531537000857 (Elsevier, Amsterdam, 2011).
59. Dmytruk, O. & Schiró, M. Gauge fixing for strongly correlated electrons coupled to quantum light. *Phys. Rev. B* **103**, 075131 https://doi.org/10.1103/PhysRevB.103.075131 (2021).
60. Landau, L. D. & Lifshitz, E. M. Quantum mechanics: non-relativistic theory, vol. 3 of *Course of Theoretical Physics*, 3rd edn. https://doi.org/10.1016/C2013-0-02793-4 (Pergamon Press, Oxford, 1977).
61. Kim, D. et al. Multimode phonon-polaritons in lead-halide perovskites in the ultrastrong coupling regime. *Nat. Commun.* **16**, 8658 https://doi.org/10.1038/s41467-025-63810-7 (2025).
62. Mornhinweg, J. et al. Mode-multiplexing deep-strong light–matter coupling. *Nat. Commun.* **15**, 1847 https://doi.org/10.1038/s41467-024-46038-9 (2024).
63. Hale, L. et al. Multi-mode deep strong coupling in a multi quantum well fabry–Pérot cavity. https://doi.org/10.1002/adom.71288 (2026).
64. De Bernardis, D., Pilar, P., Jaako, T., De Liberato, S. & Rabl, P. Breakdown of gauge invariance in ultrastrong-coupling cavity QED. *Phys. Rev. A* **98**, 053819 https://doi.org/10.1103/PhysRevA.98.053819 (2018).
65. Li, J. et al. Electromagnetic coupling in tight-binding models for strongly correlated light and matter. *Phys. Rev. B* **101**, 205140 https://doi.org/10.1103/PhysRevB.101.205140 (2020).
66. Di Stefano, O. et al. Resolution of gauge ambiguities in ultrastrong-coupling cavity QED. *Nat. Phys.* **15**, 803–808 https://doi.org/10.1038/s41567-019-0534-4 (2019).
67. Garziano, L., Settineri, A., Di Stefano, O., Savasta, S. & Nori, F. Gauge invariance of the Dicke and Hopfield models. *Phys. Rev. A* **102**, 023718 https://doi.org/10.1103/PhysRevA.102.023718 (2020).
68. Jöchl, E. et al. Absence of a superradiant phase transition in Dirac Landau polaritons. Preprint at *arXiv* https://doi.org/10.48550/arXiv.2605.27319 (2026).
69. Białek, M. et al. Hybridization of terahertz phonons and magnons in disparate and spatially-separated material specimens. *Adv. Funct. Mater.* **35**, 2416037 https://doi.org/10.1002/adfm.202416037 (2025).
70. Günter, G. et al. Sub-cycle switch-on of ultrastrong light–matter interaction. *Nature* **458**, 178–181 https://doi.org/10.1038/nature07838 (2009).
71. Riek, C. et al. Direct sampling of electric-field vacuum fluctuations. *Science* **350**, 420–423 https://doi.org/10.1126/science.aac9788 (2015).
72. Benea-Chelmus, I.-C., Settembrini, F. F., Scalari, G. & Faist, J. Electric field correlation measurements on the electromagnetic

vacuum state. *Nature* **568**, 202–206 https://doi.org/10.1038/s41586-019-1083-9 (2019).
73. Yavorskiy, D. et al. Pressure tuning of hgcdte epitaxial layers-the role of the highly disordered buffer layer. *J. Phys. D: Appl. Phys.* **58**, 025304 https://doi.org/10.1088/1361-6463/ad80a2 (2024).
74. Katsidis, C. C. & Siapkas, D. I. General transfer-matrix method for optical multilayer systems with coherent, partially coherent, and incoherent interference. *Appl. Opt.* **41**, 3978–3987 https://doi.org/10.1364/AO.41.003978 (2002).

Acknowledgements

This work was made possible thanks to high-quality MCT samples grown by molecular beam epitaxy by Nikolay N. Mikhailov and Sergey A. Dvoretsky (RAS, Novosibirsk) in 2019. We gratefully acknowledge access to this material.

Author contributions

D.Y. conceived the idea, prepared the samples, performed experiments, discussed microscopic and transfer-matrix models, discussed data interpretation, and contributed to the writing of the manuscript. D.H. developed the microscopic model, performed the corresponding calculations, discussed data interpretation, and contributed to the writing of the manuscript. N.Ch. developed the transfer-matrix model and contributed to the writing of the manuscript. Y.I. developed the experimental setup and performed experiments. A.K. performed transport measurements. Y.T. discussed microscopic and transfer-matrix models, discussed data interpretation, and contributed to the writing of the manuscript. W.K. supplied resources and contributed to the writing of the manuscript. M.B. conceived the idea, developed the experimental setup and software, discussed microscopic and transfer-matrix models, discussed data interpretation, and contributed to the writing of the manuscript.

Funding

The work was supported by the European Union through the ERC-ADVANCED grant TERAPLASM (No. 101053716). Views and opinions expressed are, however, those of the author(s) only and do not necessarily reflect those of the European Union or the European Research Council Executive Agency. Neither the European Union nor the granting authority can be held responsible for them. We also acknowledge the support of the "Centre for Terahertz Research and Applications (CENTERA2)" project (FENG.02.01-IP.05-T004/23) carried out within the "International Research Agendas" programme of the Foundation for Polish Science, co-financed by the European Union under the European Funds for a Smart Economy Programme. This work was partially supported by Pasific2 of the Polish Academy of Sciences, sponsored by the European Union's Horizon 2020 research and innovation programme under the Marie Sklodowska-Curie grant agreement No. 847639, and by the Ministry of Education and Science of Poland. This work was also partially supported by the Sonata Bis-13 2023/50/E/ST3/00584 grant of the National Science Centre of Poland. Y. T. acknowledges financial support from ERC-COG-863487 UNIQUE. This research was partially supported by the Foundation for Polish Science project "MagTop" no. FENG.02.01-IP.05-0028/23 co-financed by the European Union from the funds of Priority 2 of the European Funds for a Smart Economy Programme 2021-2027 (FENG).

Competing interests

The authors declare no competing interests.

Additional information

Supplementary information The online version contains supplementary material available at https://doi.org/10.1038/s41467-026-79076-6.

Correspondence and requests for materials should be addressed to Dmitriy Yavorskiy or Marcin Białek.

Peer review information *Nature Communications* thanks Mengkun Liu and the other, anonymous reviewer(s) for their contribution to the peer review of this work. A peer review file is available.

Reprints and permissions information is available at http://www.nature.com/reprints

Publisher's note Springer Nature remains neutral with regard to jurisdictional claims in published maps and institutional affiliations.

Open Access This article is licensed under a Creative Commons Attribution 4.0 International License, which permits use, sharing, adaptation, distribution and reproduction in any medium or format, as long as you give appropriate credit to the original author(s) and the source, provide a link to the Creative Commons licence, and indicate if changes were made. The images or other third party material in this article are included in the article's Creative Commons licence, unless indicated otherwise in a credit line to the material. If material is not included in the article's Creative Commons licence and your intended use is not permitted by statutory regulation or exceeds the permitted use, you will need to obtain permission directly from the copyright holder. To view a copy of this licence, visit http://creativecommons.org/licenses/by/4.0/.

© The Author(s) 2026

This Article in Press is shared early to give you faster access to new research. It is citable and carries a permanent DOI. The final edited version will replace it automatically.